Control of plume interference effects on axisymmetric afterbodies

Y-K Lee, S. Raghunathan and E. Benard
School of Aeronautical Engineering, Queen's University of Belfast, Belfast
UK

H-D Kim
School of Mechanical Engineering, Andong National University, Andong, Korea

T. Setoguchi
Department of Mechanical Engineering, Saga University, Saga, Japan

ABSTRACT

Plume interference effects on the axisymmetric flowfields around powered missiles are investigated using computational techniques. The study is mainly to understand the physics of the plume-induced shock and separation particularly at high plume to exit pressure ratios with and without shock-turbulent boundary layer control methods. Mass-averaged Navier-Stokes equations with the RNG k-ε turbulence model are solved using a fully implicit finite volume scheme and time-marching algorithm. The shock position and extent of separation was found to be dependent on the freestream Mach number and plume pressure ratio. Rounding the tail or a groove on the surface near the tail moved the shockwave downstream of the tail fin which should enhance the control of the missile.

NOMENCLATURE

$\mathbf{A}$	area vector
a	sound speed
C_p	specific heat at constant pressure
D	diameter of missile
E	total energy per unit mass
$\mathbf{F}$	inviscid flux vector
$\mathbf{G}$	viscous flux vector
H	total enthalpy per unit mass
k	turbulent kinetic energy
M, M_t	Mach number, turbulent Mach number
$\mathbf{Q}$	dependent vector of primitive variables
U, U_r	velocity, reference velocity
V	control volume
x_s	position of plume-induced shock
$\mathbf{\Gamma}$	preconditioning matrix
γ	ratio of specific heats
ε	turbulent dissipation rate
μ_t	turbulent viscosity
ρ, ρ_t	density, derivative of density on temperature at constant pressure
τ_{ij}	viscous stress tensor

Subscripts

0	total state
a	atmospheric state
c	combustion chamber
e	exit of supersonic nozzle
∞	freestream

1.0 INTRODUCTION

For a number of decades, though significant efforts have been made to develop missile configurations requiring a very high thrust level within a limited cross sectional area, several aerodynamic problems

Paper No. 2793. Manuscript received 30 August 2003, accepted 9 February 2004.

https://doi.org/10.1017/S0001924000000099 Published online by Cambridge University Press

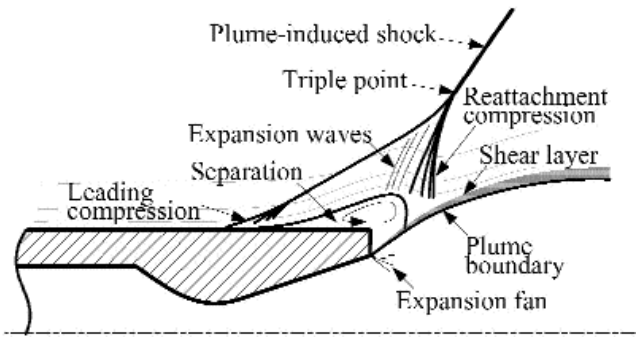


Figure 1. Schematic diagram of plume interference phenomena.

relating to powered missiles still remain because of the severely complex physics. These configurations have a highly underexpanded jet plume[1,2] downstream of the exhaust nozzle exit so that there are considerable interactions between the exhaust plume and freestream near the tail of the body. The boundary layer separation[3,4] and pitching and yawing moments that result from the interactions can have significant effects on missile stability and control[5,6].

Plume interference[7], schematically illustrated in Fig. 1, is an extremely complicated phenomenon, consisting of plume expansion which effectively produces a compression corner for the supersonic flow near the tail of the missile. As is the case for a supersonic shock-boundary layer interaction with a separation bubble, the wave system consists of a λ shock with expansion waves inside the shock reflection. The shock-induced separation near the tail of the missile where fins are normally located can have an adverse effect on control. The flow characteristics are inherently nonlinear and severely unstable during the flight at normal speeds as well as at launching. In particular, unsteady high static pressures in the separation region near the trailing edge of the body can cause unbalanced force on the missile. Therefore the control of shock-induced separation is one of the most important considerations for the effective design of powered missiles and flight vehicles.

Most of the knowledge base on plume-freestream interactions on afterbody surfaces of powered missiles is from wind tunnel tests. Salmi[8] and Hinson *et al*[9,10] examined the effects of underexpanded jet plumes on the static stability of missile bodies at supersonic speed. They concluded plume interference effects could alter the pressure distribution on the aft surface of a missile body resulting in changes in the aerodynamic forces and moments acting on it. McGhee *et al*[11-13] performed experiments on the effects of jet plume-induced flow separation on several axisymmetric bodies with various forebody and afterbody geometries at supersonic speeds. Their main conclusion was that at relatively lower freestream Mach numbers, separation regions were small and the jet pressure ratio required to induce the separation was relatively lower than when compared with results at higher Mach numbers. Wu *et al*[14-16] made investigations into transonic flowfields around various bodies of revolution with and without plumes. Their investigation showed that viscous effects on the tested model surfaces were not significant but crucial on the boat-tailed region.

A detailed understanding of plume-interference phenomena for an arbitrary missile model is indispensable to missile design. However, the current knowledge base built in this research area is not adequate to provide an overall insight into the physics involved. CFD (Computational Fluid Dynamics) analyses, therefore, offer a way forward for the development of such a design. Very recently, some computational work[17,18] has been made mainly on base flow problems but, to the authors' knowledge, no CFD study has been conducted for the control of plume interference phenomena.

In the current research, CFD studies were conducted for missile models with simple, rounded and grooved afterbodies to simulate moderately and highly underexpanded exhaust plumes mainly at supersonic speeds. A fully implicit finite volume scheme was applied to mass-averaged Navier-Stokes equations with a two-equation turbulence model, RNG k-ε. The present numerical study may develop a basic understanding into the influence of rounded and grooved afterbodies on the plume-induced shockwave and separation, leading to the effective and efficient control of flight bodies.

2.0 MODEL CONFIGURATION

Figure 2 shows the schematic diagrams of missile models tested in this CFD analysis. The present computational model can be basically represented as an ogive forebody and straight afterbody without tail fins, identified as Model Simple. The 13-calibre missile body for the code validation had a four-calibre tangent ogive nose and a cylindrical afterbody diameter of 63·5mm. A convergent-divergent nozzle, having a design Mach number of 2·7, an exit diameter of D_e = 50·9 mm and a divergence angle of 20°, was used to acquire supersonic plumes downstream of the nozzle exit. Two rounded afterbodies with different non-dimensional radii of rounding, R/D = 0·1 and 0·2, designated as Model R6·3 and R12·6, were tested to examine the rounding effects on the flow features of plume-freestream interactions. The grooving effects on the plume interference were examined with Model G02 and G05, which have 0·2% L and 0·5% L of the width of the groove respectively, in order to find an effective method of controlling the flow features which may adversely affect overall missile performance.

3.0 NUMERICAL SIMULATIONS

3.1 Governing equations

The system of mass averaged, time-dependent Navier-Stokes equations governing the flowfields around missiles is given in conservation form. The resulting equations are expressed in integral form for an arbitrary control volume V with differential surface area dA,

$$\mathbf{\Gamma}\frac{\partial}{\partial t}\int_V \mathbf{Q}\,\mathrm{d}V + \oint[\mathbf{F}-\mathbf{G}]\cdot\mathrm{d}\boldsymbol{A} = 0 \qquad \ldots (1)$$

where **F** and **G** are inviscid and viscous flux vectors in standard conservation form and **Q** is the dependent vector of primitive variables.

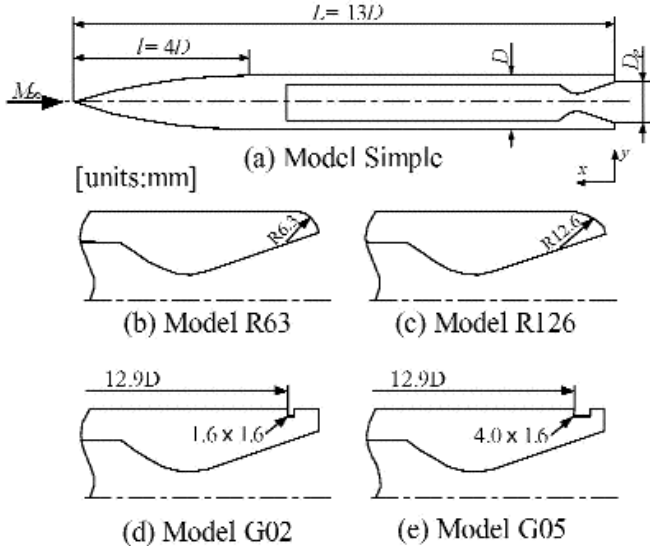


Figure 2. Testing models and afterbody configurations.

https://doi.org/10.1017/S0001924000000099 Published online by Cambridge University Press

$$\mathbf{F} = \begin{bmatrix} \rho \mathbf{v} \\ \rho \mathbf{v} v_x + p\hat{i} \\ \rho \mathbf{v} v_y + p\hat{j} \\ \rho \mathbf{v} v_z + p\hat{k} \\ \rho \mathbf{v} H \end{bmatrix}, \quad \mathbf{G} = \begin{bmatrix} 0 \\ \tau_{xi} \\ \tau_{yi} \\ \tau_{zi} \\ \tau_{ij} v_j + \mathbf{q} \end{bmatrix}, \quad \mathbf{Q} = \begin{bmatrix} p \\ v_x \\ v_y \\ v_z \\ T \end{bmatrix} \qquad \ldots (2)$$

In Equation (2), H is total enthalpy per unit mass, which is related to the total energy per unit mass E by $H = E + p/\rho$, where E includes both internal and kinetic energy, and $\mathbf{q}$ is the heat flux vector. The preconditioning matrix Γ is included in Equation (1) to provide more accurate velocity and temperature gradients in viscous fluxes, and pressure gradients in inviscid fluxes. The advantage of the preconditioning treatment[19] in the calculations allows the propagation of acoustic waves in the system to be singled out. This matrix is given by

$$\mathbf{\Gamma} = \begin{bmatrix} \theta & 0 & 0 & 0 & \rho_T \\ \theta v_x & \rho & 0 & 0 & \rho_T v_x \\ \theta v_y & 0 & \rho & 0 & \rho_T v_x \\ \theta v_z & 0 & 0 & \rho & \rho_T v_x \\ \theta H - \delta & \rho v_x & \rho v_x & \rho v_x & \rho_T H + \rho C_p \end{bmatrix} \qquad \ldots (3)$$

where ρ_T is the derivative of density with respect to temperature at constant pressure and $\delta = 1$ for compressible flow. The parameter θ is defined as

$$\theta = \left(\frac{1}{U_r^2} - \frac{\rho_T}{\rho C_p} \right) \qquad \ldots (4)$$

In Equation (4), the reference velocity U_r is chosen such that the eigenvalues of the system remain well conditioned with respect to the convective and diffusive timescales, and C_p is the specific heat at constant pressure.

A two-equation turbulence model, RNG k-ε modified to take account of compressibility effects, was employed to close the governing equations. The turbulent Mach number used in the dilatation term of the turbulence model is identified as $M_t = (k/a^2)^{0.5}$. The model for the turbulent viscosity μ_t is written as $\mu_t = \rho C_\mu (k^2/\varepsilon)$, where the turbulent kinetic energy k and dissipation rate ε are solved from the turbulent transport theory. The following model constants are used: $C_\mu = 0{\cdot}0845$, $C_{1\varepsilon} = 1{\cdot}42$, $C_{2\varepsilon} = 1{\cdot}68$.

3.2 Numerical schemes

The present investigation adopted a commercial computational code, Fluent 5, in order to analyse complex compressible flows around missile bodies. This CFD code has the ability to predict flowfields involving strong shock interactions with shear layers and boundary layers and is expected to provide high quality simulations for the flowfield around a missile body with a highly underexpanded plume.

The governing equations are discretised spatially using a fully implicit finite volume scheme, in which the physical domain is subdivided into numerical cells and the integral equations are applied to each cell. The flowfield is represented by associating a distinct value of the discretised solution vector with each control volume, which is used to evaluate the fluxes at cell faces. The solution vector is computed using a multidimensional linear reconstruction approach[20], which enables higher-order accuracy to be achieved at the cell faces through a Taylor series expansion of the cell-averaged solution vector. The use of a second order accurate scheme makes it feasible to capture the shock structure and the boundary-layer flows near the wall region, but only by using fine computational grids. With respect to temporal discretisation, an explicit multi-stage time stepping scheme[21] is used to discretise the time derivatives in the governing equations. Then it is assumed that time marching proceeds until a steady state solution is reached.

To acquire accurate solutions, CFD analyses must be conducted by using a proper computational domain and grid quality in consideration of the flow features to be expected especially in missile aerodynamics. In the present computation, grid adaptation and higher order approximation schemes were used to get more reliable results. A second order accurate scheme was selected to correctly capture the flow features with strong pressure gradients such as various shock structures, shear layers and plume boundaries, and the wake flow downstream of the afterbody of missile models.

The code was validated for the missile model with a sharp edge under several test conditions with available results of previous wind tunnel tests[22]. Some representative results of the code validation will be discussed in the results section.

3.3 Computational grids

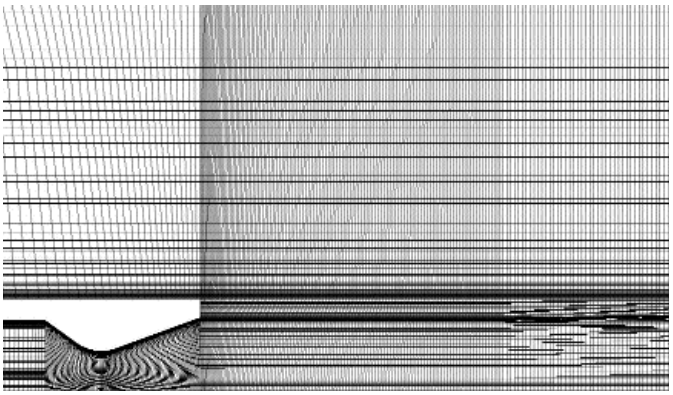
Figure 3a shows the detailed layout of the grids near the afterbody edge and exhaust jet region. The computational domain was chosen to take account of the large plume expansion at high pressure ratios. The shockwaves and mixing layers are very thin and the convergence of solutions strongly depends on plume dimensions and locations of shockwaves inside the plume and on the afterbody. Therefore grids were clustered in regions with large gradients, such as shockwaves, shear layers, and boundary layers to provide more accurate predictions of the flowfield. For some cases with a highly underexpanded plume, grid adaptation was applied to the regions with plume boundaries and shockwaves when coarse grids were there.

The fineness of computational grids required to obtain grid independent solutions was first examined for some of the flowfields under consideration. Figure 3(b) shows a typical result of grid convergence tests for a flight condition of $p_c/p_a = 341{\cdot}8$ and $M_\infty = 2{\cdot}0$, which produces the largest plume dimensions among tested cases at supersonic speeds. The continuity residuals given here are converged values for each grid size when the mass imbalance for inlet, outlet and freestream boundaries became approximately unchangeable. For the several testing grid systems, Fig. 3c shows a grid fineness test result with the velocity profiles acquired at the afterbody edge. When about 140,000 nodes were used, consequently, the solution for the given flight condition was considered correct because there was no change observed not only in the residual but also in the velocity profile with a further increase in the grid size. The grid fineness for the models with rounded or grooved afterbodies was judged by using the same approach and about 150,000 nodes were fine enough for all cases tested.

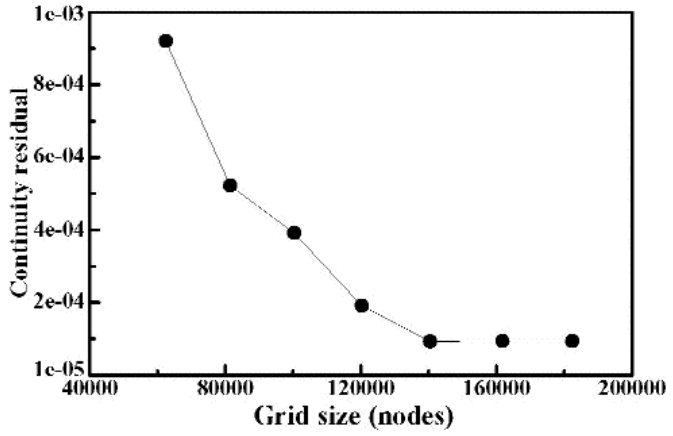
3.4 Boundary conditions and analysis

Axisymmetric plume flowfields were initiated from highly compressed air in the combustion chamber and expanded to supersonic external flowfields through the converging-diverging nozzle. The expansion occurred according to the plume pressure ratio, which is the ratio of chamber total pressure p_c to atmospheric pressure p_a. The mass flow boundary condition was applied to the combustion chamber inlet, where p_c was adjusted to achieve the velocity needed to provide the prescribed mass flux at the boundary. The pressure far-field condition was used for the half-parabolic boundary enclosing the model to specify freestream conditions at infinity with the freestream Mach number and static conditions. This condition uses the Riemann-invariants to determine the flow variables at the boundary. The pressure outlet boundary condition was applied to the vertical boundary at the end of the computational domain with only static pressure specified.

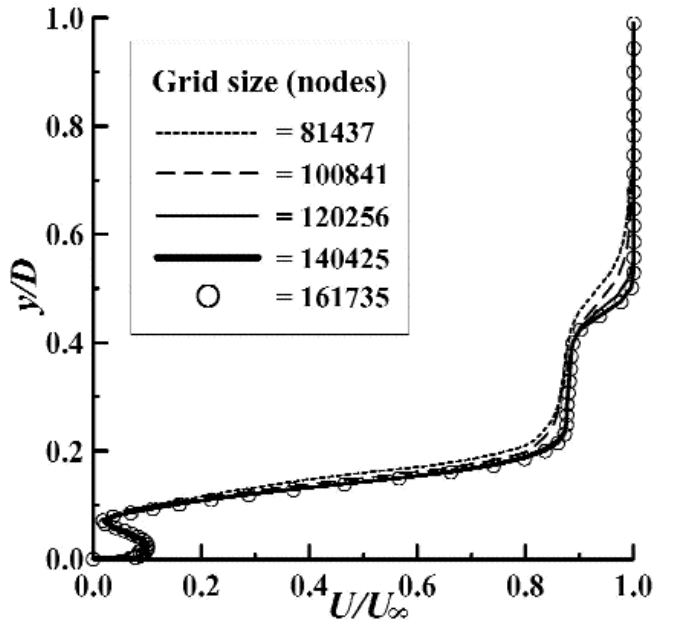
https://doi.org/10.1017/S0001924000000099 Published online by Cambridge University Press



(a)



(b)



(c)

Figure 3 Grid system and convergence at p_c/p_a = 341·8 and M_∞ = 2·0: (a) Structural grids near the simple afterbody, (b) Grid convergence with the continuity residual, (c) Grid fineness tests with velocity profiles at the afterbody edge.

The main parameters to characterise plume-freestream interactions were the plume pressure ratio p_c/p_a and freestream Mach number M_∞ in the range of 50~350 and 1·2~3·0 respectively. These ranges covered moderately to highly underexpanded plumes embedded in supersonic external flows. For simplicity, the effect of total temperature was not taken into account. Freestream pressure and temperature were assumed to be constant with values of 1 atm and 288·15K respectively. With a proper grid size chosen by using the approach explained through Fig. 3, basically, solutions were considered converged when the residuals for all equations drop by three orders of magnitude, typically 10^{-4} as shown in Fig. 3(b), with the mass imbalance check for flow inlet and outlet boundaries.

4.0 RESULTS

Figure 4 shows the result of code validations as wall static pressure distributions with distance x, where x is measured from the end of the afterbody surface towards upstream. Distances are normalised by the missile diameter D and local static pressures along the missile surface are normalised by the atmospheric pressure p_a. All pressure distributions in this paper follow this convention. The results show reasonable agreement with the limited available pressure measurements taken from a past wind tunnel experiment[22]. There are differences in the pressure values in the compression region before the plume and these could be attributed to the inability of CFD code to estimate accurately the sharp pressure rise in this region. The differences between the computed and measured pressure values upstream of the sharp pressure rise at M_∞ = 1·2 can be attributed to support strut-plume interference and blockage effects in the wind tunnel tests.

Figures 5 and 6 show the influences of the freestream Mach number on the flowfield around the model with a sharp corner — to be used as the reference model. The results shown here are for a fixed

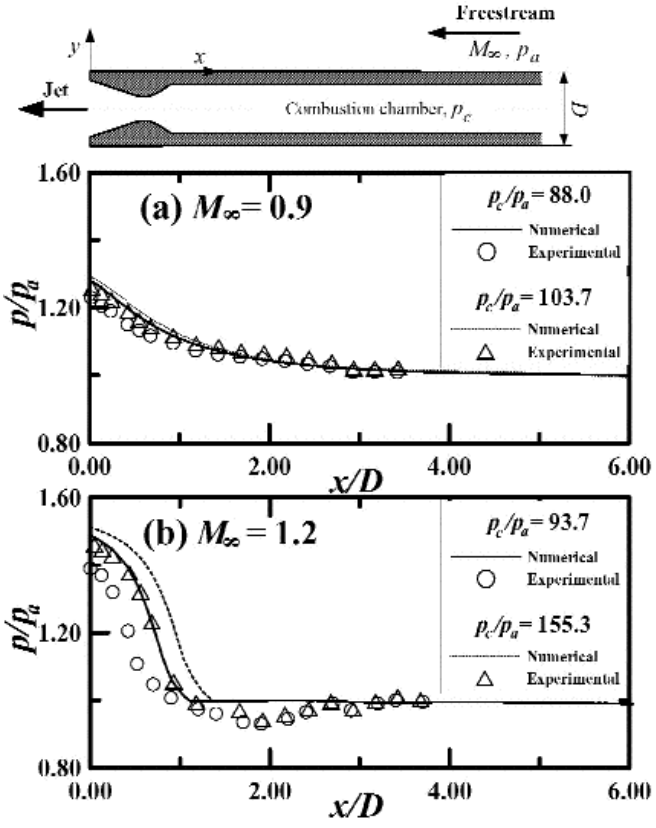


Figure 4 Validation of the present results with wind tunnel tests.

https://doi.org/10.1017/S0001924000000099 Published online by Cambridge University Press

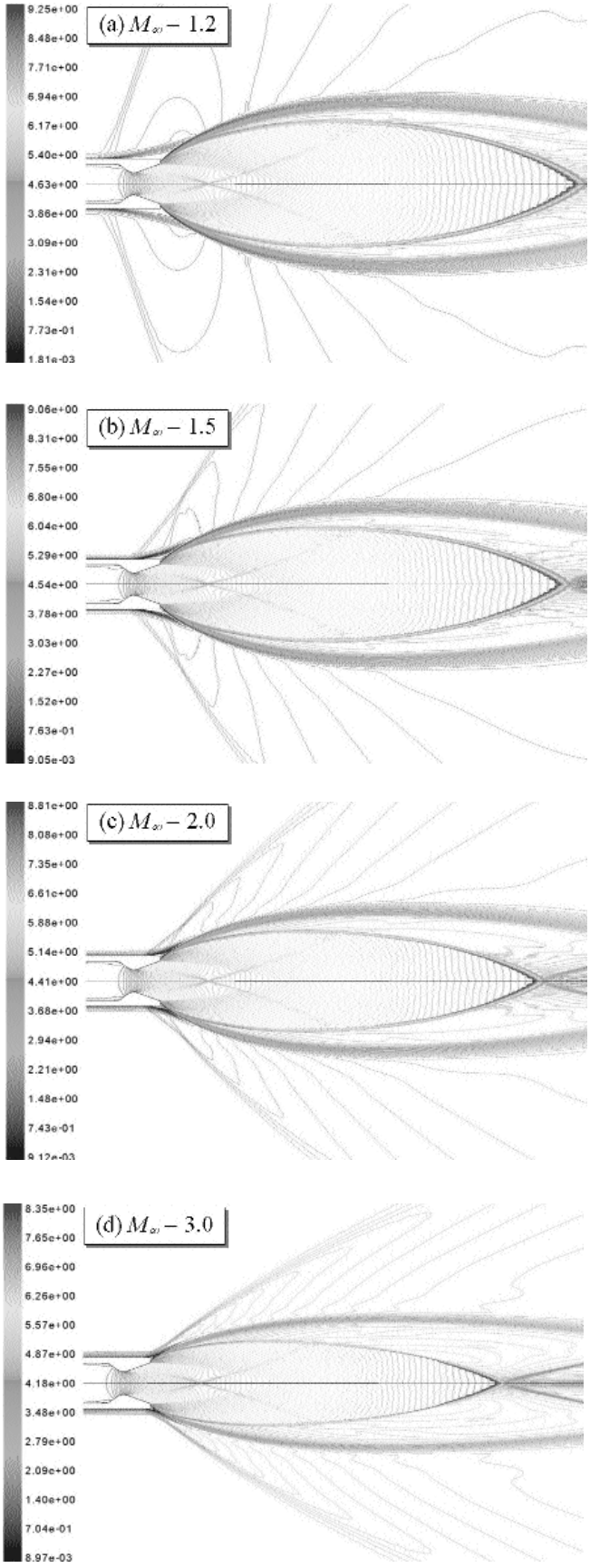


Figure 5. Mach number contours around the simple model for various freestream Mach numbers at p_c/p_a = 170·9.

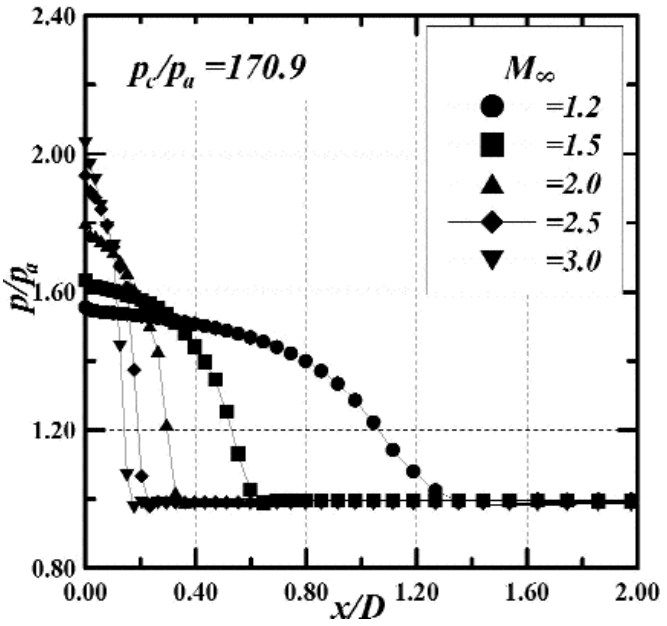


Figure 6. Effect of the freestream Mach number on wall pressure distributions at p_c/p_a = 170·9.

pressure ratio p_c/p_a = 170·9 and at supersonic freestream. It is observed (Fig. 5(a)) that leading compression waves before the wall boundary separation and reattachment compression waves coalesce into the plume-induced shockwave. As the freestream Mach number increases, the higher dynamic energy of freestream may more strongly restrict the expansion of the plume. Thus, it can be observed that the expansion angle of supersonic plume is reduced and the plume-induced shock moves downstream. It is also interesting to note that, at M_∞ = 3·0 (Fig. 5(d)), the λ-shaped shock changes into a single oblique shock with reduced boundary layer separation. It implies, during an acceleration of supersonic missiles up to its normal speed, there can be a significant change in the interaction features near the base, consequently making the flight very unstable.

The location of the shock and the spread of shock system can be observed from the pressure distribution near the tail of the missile (Fig. 6). With an increase in the freestream Mach number, the shock becomes stronger and the extent of shock interaction is reduced as the shock approaches the afterbody edge of the model. Therefore, a further increase in the flight Mach number would give an insignificant shock movement to the downstream.

Figure 7 shows, for a fixed M_∞ = 2·0, the effects of the plume pressure ratio on the overall flow features around Model Simple (sharp corner). As the plume pressure ratio increases, there is a stronger expansion through the nozzle so that the plume dimensions in angle and length are significantly increased. This should result in the upstream movement of both plume-induced shock and boundary layer separation near the afterbody edge. Further, as observed from the pressure distributions (Fig. 8), an increase in the plume pressure ratio increases the shock strength and length of the shock interaction region.

The extent of the shock movement with the increase in the plume pressure ratio can be seen from Fig. 9. The results shown here are for two freestream Mach numbers of 1·2 and 2·0. For the lower Mach number, when the pressure ratio is increased from 51·3 to 265·4, the shock moves by a distance $\Delta x_s/D$ of 1·25 while the corresponding motion at a higher Mach number of 2 is 0·55. It implies that the changes in the plume pressure ratio have lesser influence on fin control in flight at higher Mach numbers.

https://doi.org/10.1017/S0001924000000099 Published online by Cambridge University Press

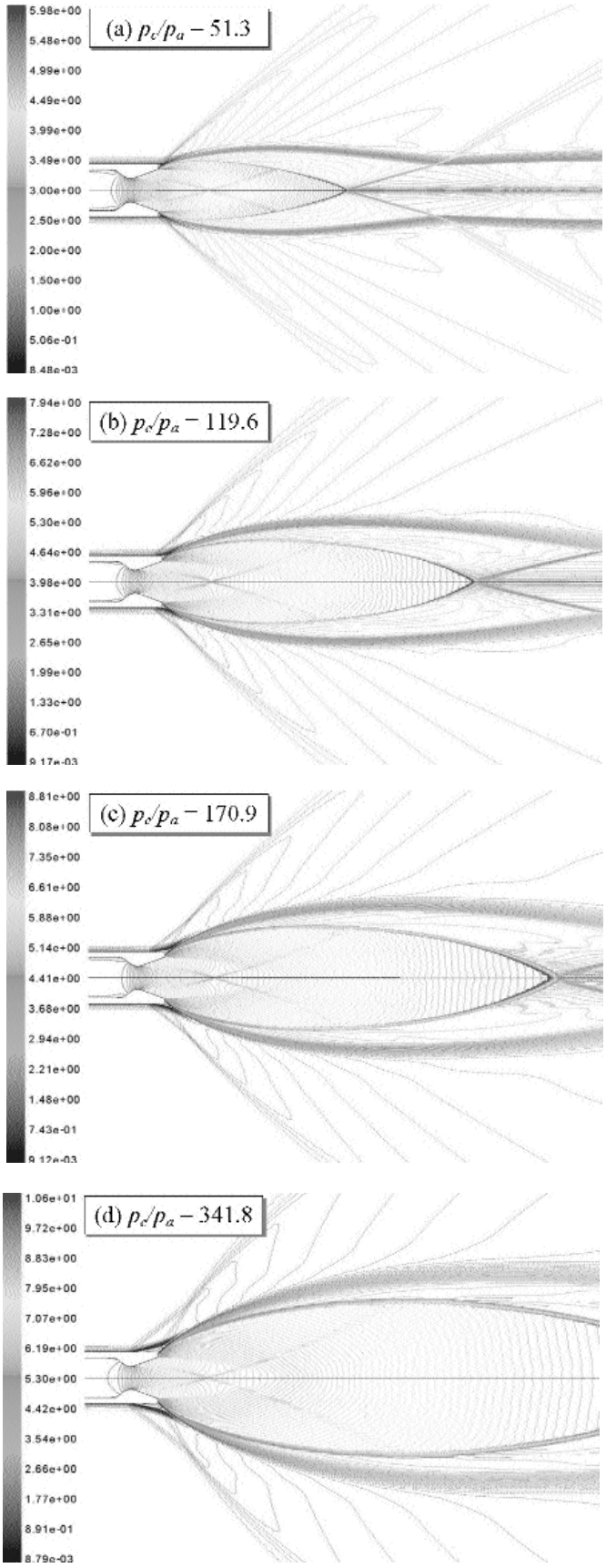


Figure 7. Mach number contours around the simple model for various plume pressure ratios at M_∞ = 2.0.

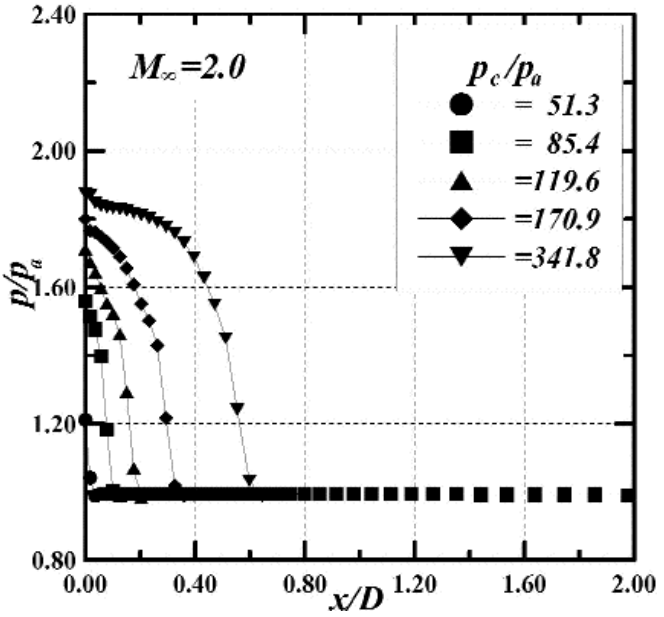


Figure 8. Effect of the plume pressure ratio on wall pressure distributions at M_∞ = 2·0.

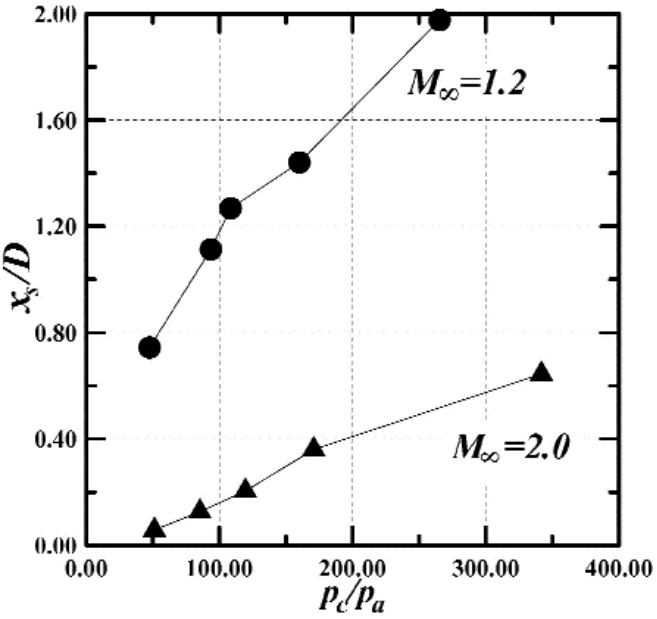


Figure 9. Effect of the plume pressure ratio on the position of plume-induced shock at M_∞ = 1·2 and 2·0.

The effects of rounded corners at the base of the missile on the flowfield are shown in Figs 10 to 13. The results shown here are for two radii of curvature R/D = 0·1 (R63) and 0·2 (R123). When compared with the body with sharp corners (Fig. 5), the rounded corners do produce a change in the shock structure inside the plume particularly at low Mach numbers (Fig. 10). With a rounded corner, the barrel shock reflects as a normal shock (Fig. 10(a)) through wave reflections. This should reduce the dynamic energy of the flow in the succeeding wave cells. An increase in the Mach number has a larger effect on the shock structure (Fig. 10). However, as was the case for the body with a sharp corner, an increase in the Mach number results in the upstream movement of the barrel shock and the downstream movement of the plume-induced shock. For a given Mach number and with an increase in the pressure ratio, there are no significant

https://doi.org/10.1017/S0001924000000099 Published online by Cambridge University Press

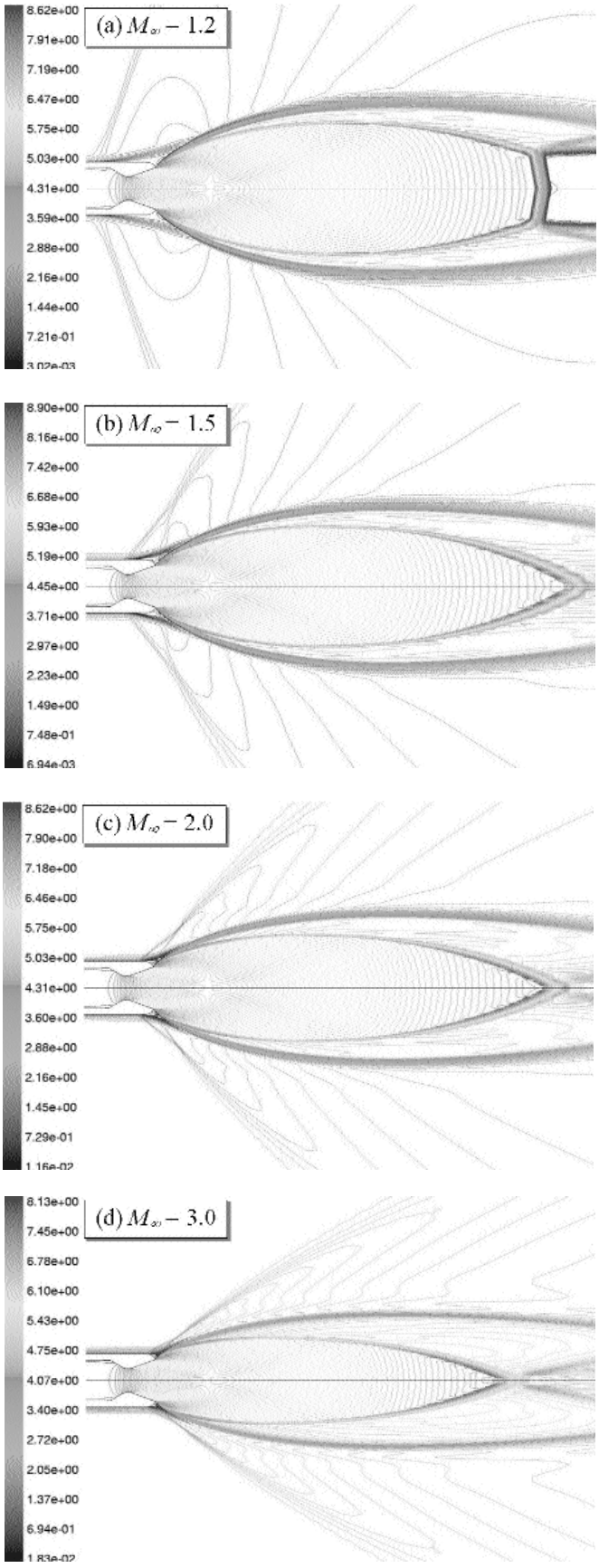


Figure 10. Mach number contours around Model R126 for various freestream Mach numbers at p_c/p_a = 170·9.

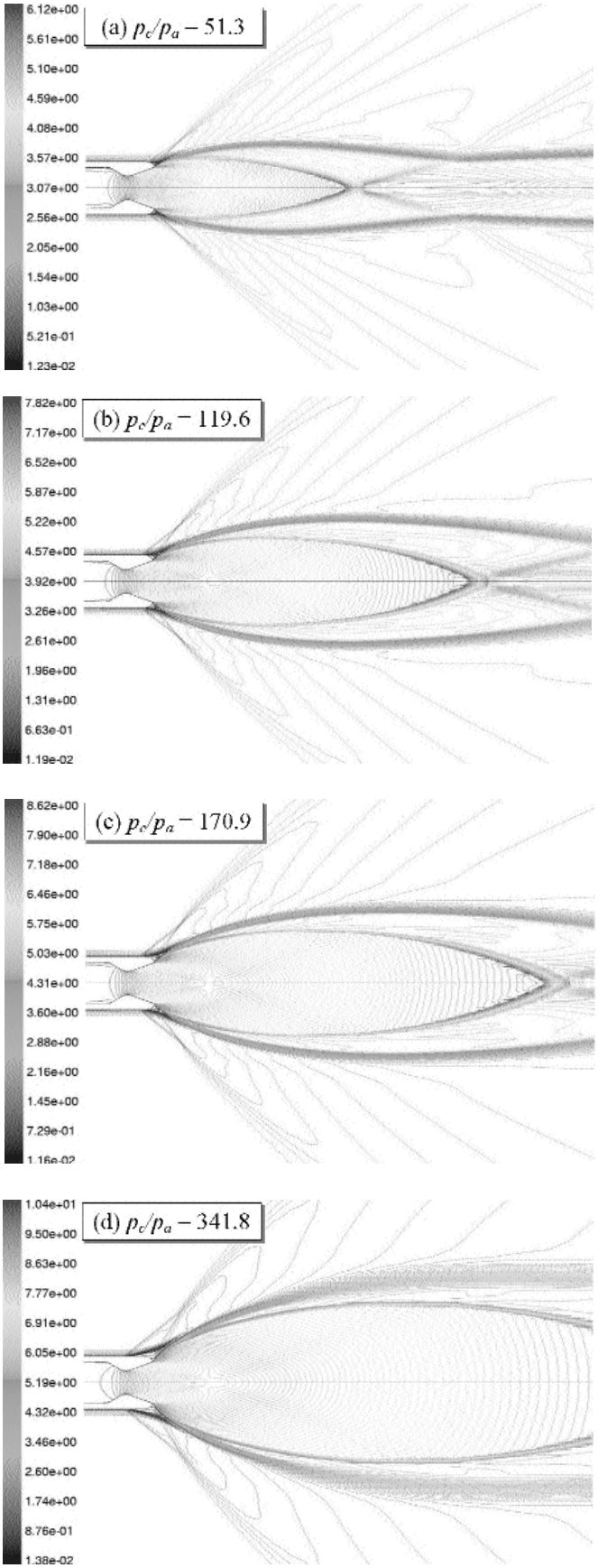


Figure 11. Mach number contours around Model R126 for various plume pressure ratios at M_∞ = 2·0.

https://doi.org/10.1017/S0001924000000099 Published online by Cambridge University Press

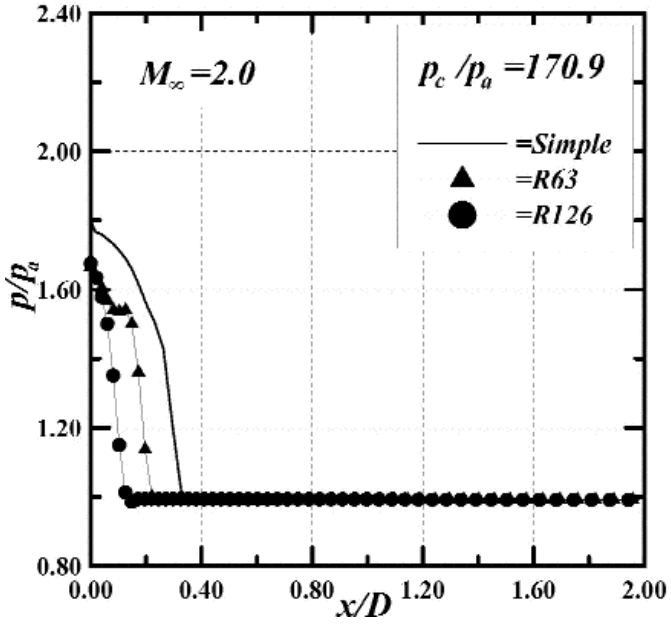


Figure 12. Effect of the rounded trailing edge on pressure distributions at p_c/p_a = 170·9 and M_∞ = 2·0.

differences in the flowfield between bodies with sharp (Fig. 7) and rounded corners (Fig. 11).

For a given freestream Mach number and pressure ratio, the pressure distributions on the missile body show that increasing the radius of curvature at the base of the body reduces the shock strength and moves the shock aft (Fig. 12). The reason for this could be the increased range of wave interactions between the λ shock system and expansion waves produced on the larger rounded edge for the given flight condition. The change in the radius of curvature has a relatively larger effect on shock positions at lower supersonic Mach numbers (Fig. 13(a)). The variation of shock positions with the pressure ratio is approximately linear for all three configurations tested (Fig. 13(b)). At a higher pressure ratio p_c/p_a = 341·8 with a rounded afterbody model (R/D = 0·2), there is a change in shock positions of about 0·23 calibres rearwards when compared with the simple afterbody model.

The effect of a groove in the vicinity of plume-induced shock interaction on the flowfield can be observed from Figs 14~17. The groove produces compression waves at its location (Figs 14 and 15). Mach number contours at several supersonic speeds and for a fixed pressure ratio of 170·9 indicate that the groove has a large effect on the plume with the appearance of a normal shock at the end of the barrel wave system for lower Mach numbers (Fig. 14). The changes in the flowfield produced are less rapid when compared to the model with a rounded base (Fig. 10). Generally, an increase in the pressure ratio (Fig. 15) produces similar effects to those on Model Simple (Fig. 5) and the model with rounded base (Fig. 11).

As regards the shock position at a pressure ratio of 170·9, the change in the width of the groove has negligible effects at most Mach numbers (Fig. 17(a)). At M_∞ > 2·0, the variation in shock positions is within $\Delta x_s/D$ = 0·05 for a change in groove width of 0·3% L. At larger pressure ratios (Fig. 17(b)), the increase in groove width has an adverse effect on the shock position (Figs 16 and 17(b)) in the sense that the shock moves upstream. Typically, at higher pressure ratios of p_c/p_a > 170, the introduction of a groove can change the shock position by 0·2 calibres or more.

The following results (Figs 18-19) can summarise the effectiveness of the passive methods used to control the plume-induced shock and shock-induced separation.

Figures 18 and 19 show iso-Mach number plots presenting the effect of afterbody shape on the plume interference for the fixed plume

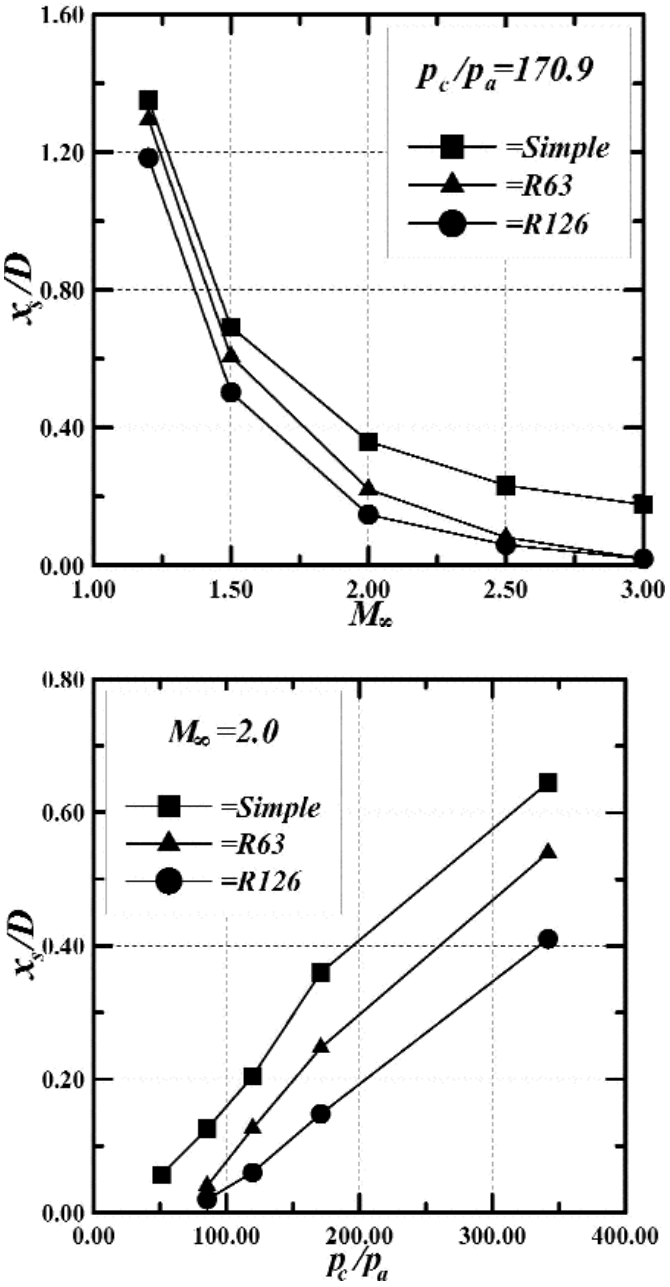


Figure 13. Comparison of shock positions between simple and rounded trailing edges: (a) For various Mach numbers, (b) For various plume pressure ratios.

pressure ratio at M_∞ = 2·0 and 3·0 respectively. The wave structures inside and outside the plume are strongly dependent on the initial expansion of the plume and the shape of trailing edge (Fig. 18). Even the small change of afterbody shape changes the plume expansion as well as the physics of wave interactions near the trailing edge. However, when the plume-induced shock forms almost at the afterbody edge of the model (Fig.19(a)), a flow control has an insignificant effect on the flowfield.

The effects of controls on pressure distributions are shown in Fig. 20. Both control methods, Model R63 and G02, give rise to a downstream movement of the plume-induced shock of nearly 0·2 calibres. The shock strength is reduced with afterbodies having rounded corners, while it is not significantly changed by the presence of a groove for the given flight condition.

https://doi.org/10.1017/S0001924000000099 Published online by Cambridge University Press

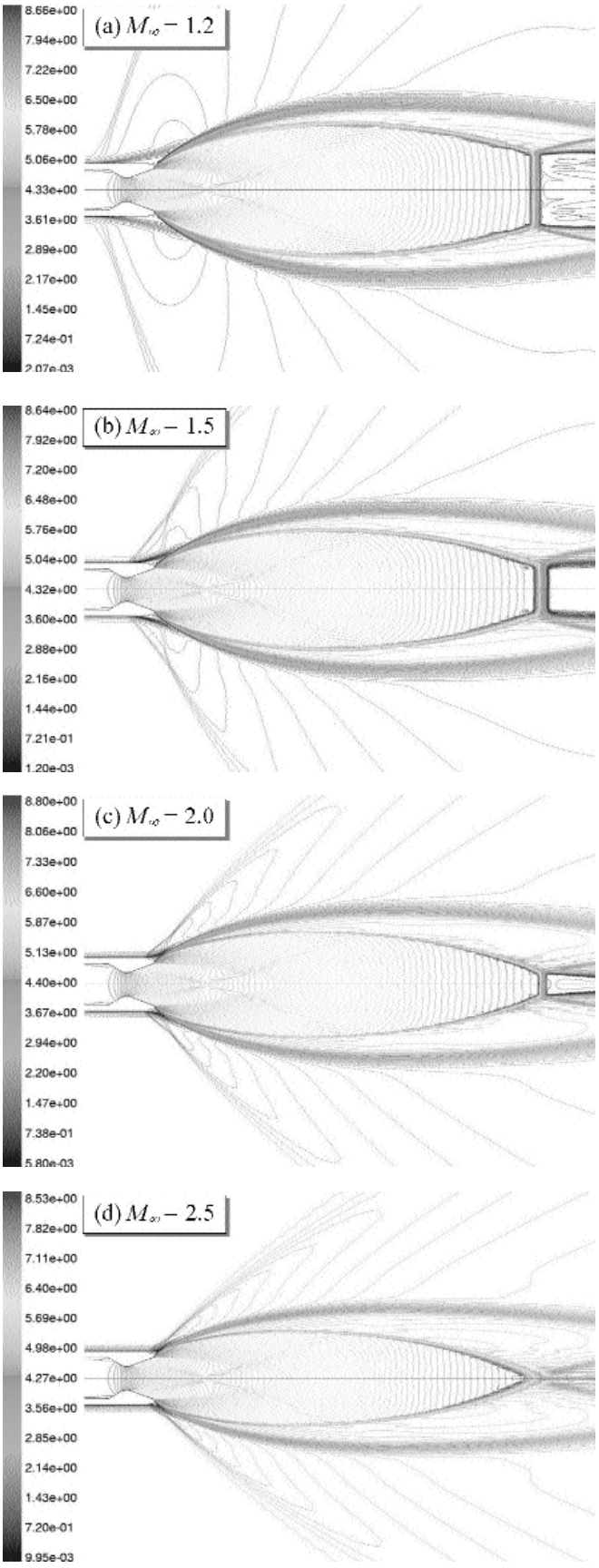


Figure 14. Mach number contours around Model G05 for various freestream Mach numbers at p_c/p_a = 170·9.

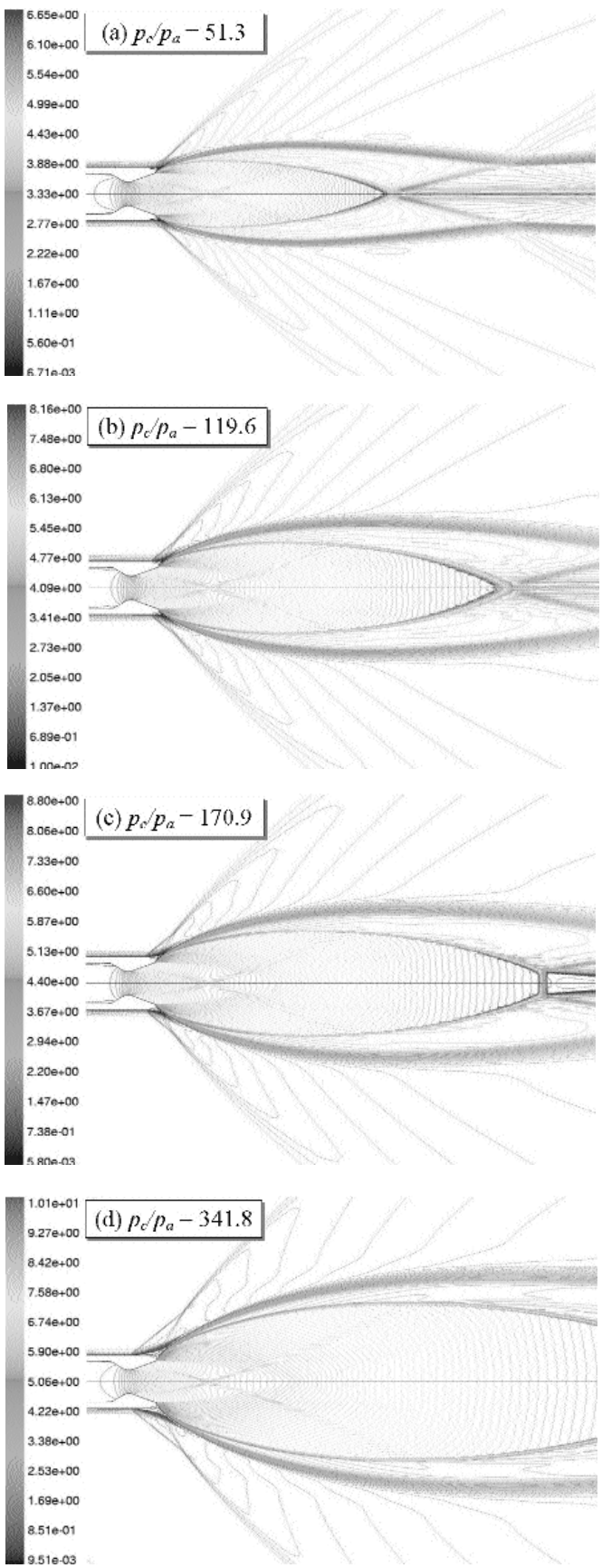


Figure 15. Mach number contours around Model G05 for various plume pressure ratios at M_∞ = 2·0.

https://doi.org/10.1017/S0001924000000099 Published online by Cambridge University Press

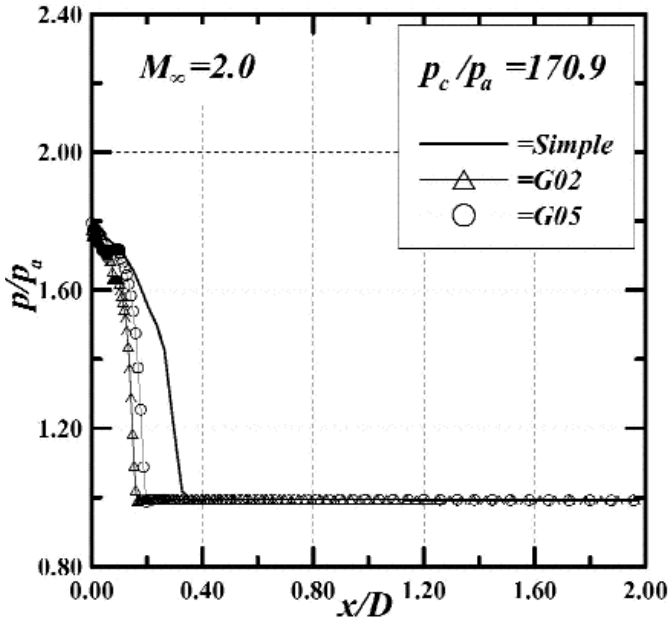
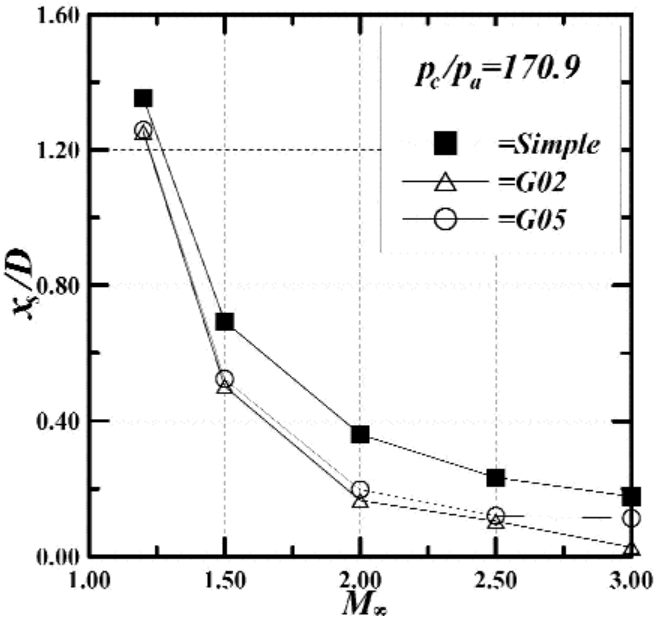
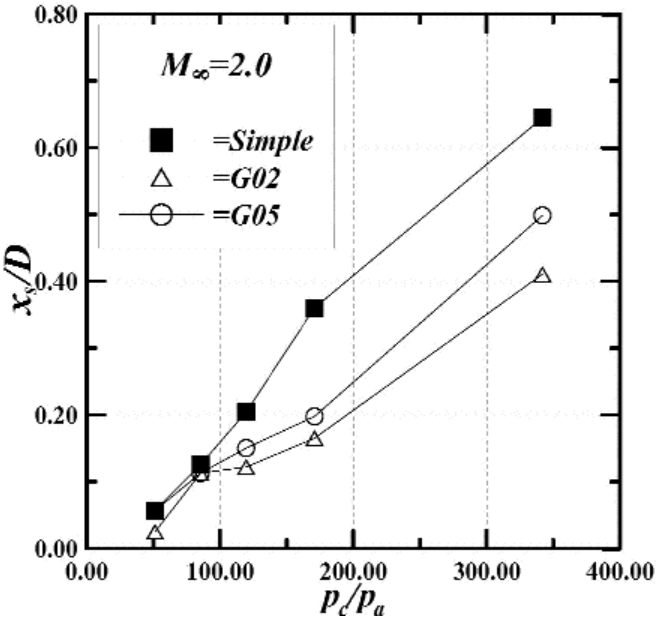


Figure 16. Effect of the grooved trailing edge on pressure distributions at p_c/p_a = 170·9 and M_∞ = 2·0.



(a)



(b)

Figure 17. Comparison of shock positions between simple and grooved trailing edges: (a) For various Mach numbers, (b) For various plume pressure ratios.

Both control configurations produce similar effects on shock positions with the increase in the Mach number (Fig. 21(a)). In contrast, the control with a groove has a larger effect in moving the shock rearwards with the increase in the plume pressure ratio (Fig. 21(b)). It is interesting to note that at lower pressure ratios of $p_c/p_a < 100$, a grooved afterbody does not give improved performance in shock control.

5.0 CONCLUSIONS

Plume interference effects on axisymmetric supersonic flowfields around missile bodies have been investigated computationally. Mass-averaged Navier-Stokes equations with the RNG k-ε turbulence model were solved using the fully implicit finite volume scheme and time-marching algorithm. An understanding of the physics of the plume-induced shock and separation was developed particularly at high plume pressure ratios with and without shock-turbulent boundary layer control methods. To characterise moderately to highly underexpanded plumes imbedded in supersonic flows, the plume pressure ratio was varied in the range of 50~350 at flight Mach numbers of 1·2~3·0.

Generally, an increase in the freestream Mach number introduced a stronger plume-induced shock and a reduced extent of shock interaction as the shock moves downstream. On the other hand, an increase in the plume pressure ratio led to the opposite characteristics except strengthening the shockwave. The control methods with a rounded tail or groove on the surface of the body near the tail produced positive effects in moving the plume-induced shock downstream and therefore alleviating the plume interference effects on the fin site.

REFERENCES

1. ALBINI, F.A. Approximate computation of under-expanded jet structure, *AIAA J,* 1965, **3,** (8), pp 1538.
2. BOYNTON, F.P. Highly under-expanded jet Structure: exact and approximate calculations, *AIAA J,* 1967, **5,** (9), pp 1703-1704.
3. ADAMSON, T.C. and NICHOLLS, J.A. On the structure of jets from highly underexpanded nozzles into still air, *J Aeronaut Sciences*, 1959, **26**, pp 16-24.
4. ALPINIERI, L.J. and ADAMS, R.H. Flow separation due to jet pluming, *AIAA J,* 1966, **4,** (10), pp 1865-1866.
5. FETTERMAN, D.E. Effects of simulated rocket-jet exhaust on stability and control of a research-type airplane configuration at a Mach number of 6·86, 1959, NASA TM X-127.
6. YANOWITCH, S. and HNEUBER, R.N. Scout first stage flight characteristics, 1968, NASA CR-111945.
7. RAGHUNATHAN, S., KIM, H.D., BENARD, E., MALLON, P. and HARRISON, R. Plume interference effects on missile bodies, Jan 2001, 39th AIAA Aerospace Sciences Meeting, Reno NV, AIAA-2001-0259.
8. SALMI, R.J. Effects of jet billowing on stability of missile-type bodies at Mach 3·85, June 1960, NASA TN D-284.

https://doi.org/10.1017/S0001924000000099 Published online by Cambridge University Press

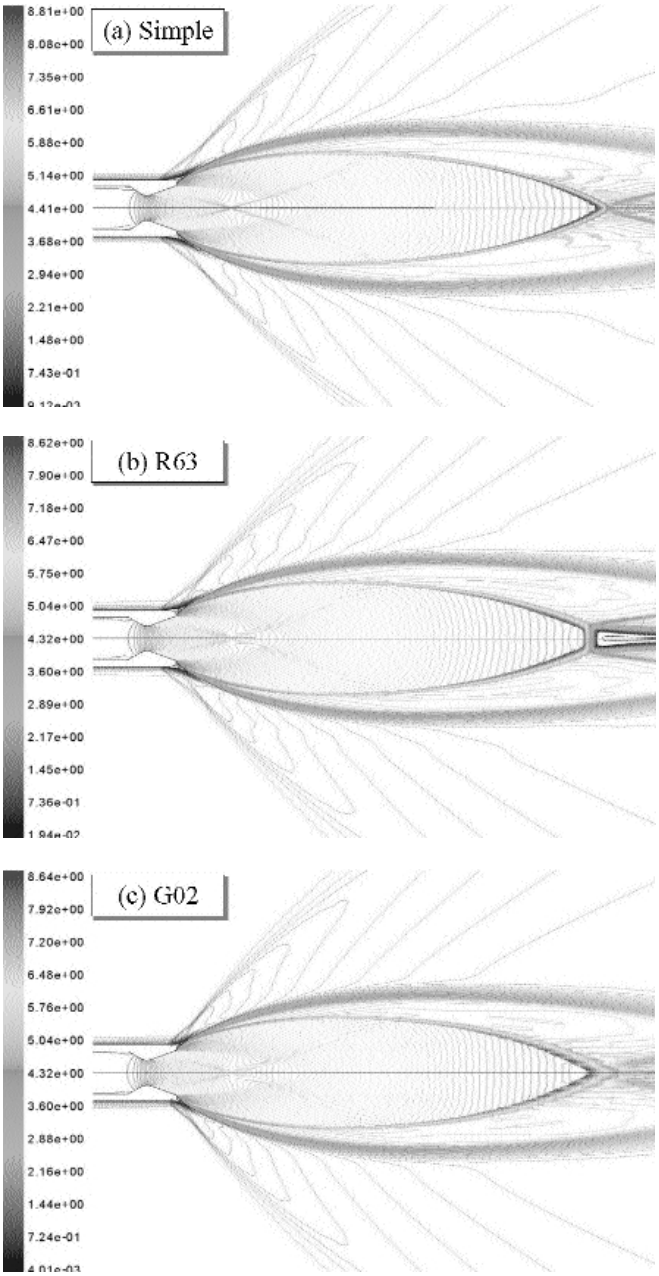


Figure 18. Mach number contours for various afterbodies at p_c/p_a = 170·9 and M_∞ = 2·0.

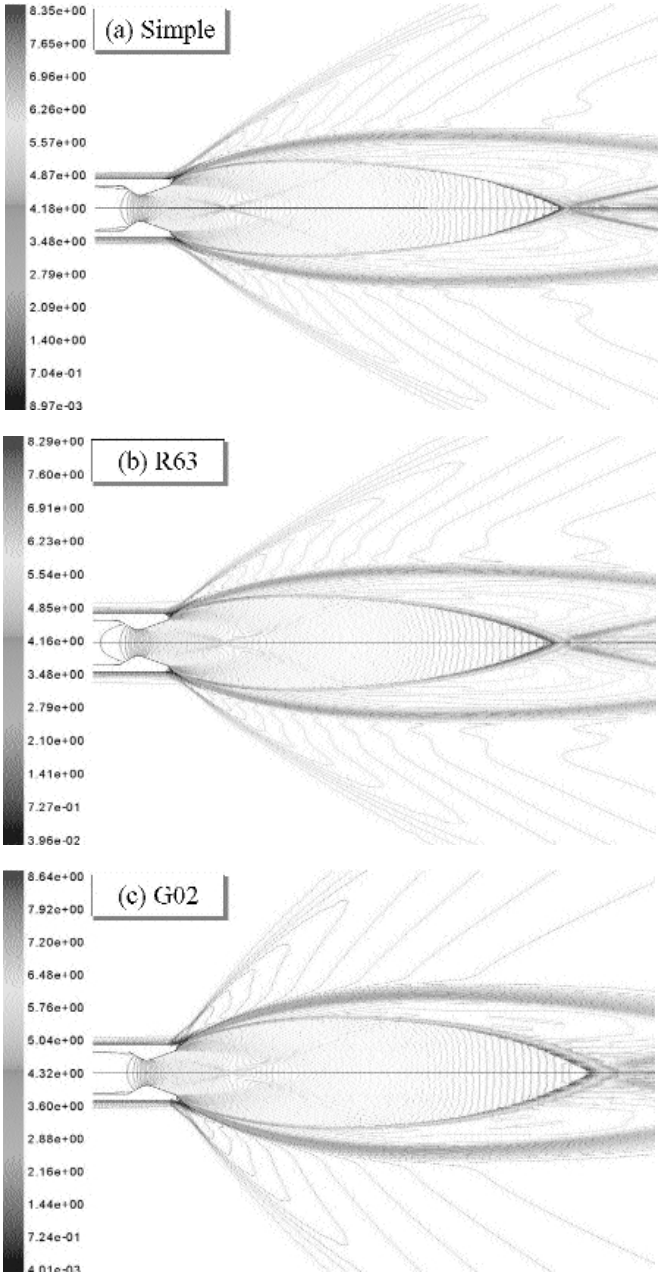


Figure 19. Mach number contours for various afterbodies at p_c/p_a = 170·9 and M_∞ = 3·0.

9. HINSON, W.F. and MCGHEE, R.J. Effects of jet pluming on the static stability of five rocket models at Mach number of 4, 5 and 6 and Static-Pressure Ratios up to 26,000, 1967, NASA TN D-4064.
10. HINSON, W.F. and FALANGA, R.A. Effects of jet pluming on the static stability of cone-cylinder-flare configurations at Mach number of 9·64, 1969, NASA TN D-1352.
11. MCGHEE, R.J. Some effects of jet pluming on the static stability of ballistics bodies at a Mach number of 6·00, 1966, NASA, TN D-3698.
12. MCGHEE, R.J. and MARTIN, J.A. Exploratory investigation of flow field resulting from forward-facing nozzles exhausting near a large cylindrical body at free-stream Mach numbers of 3·0 to 6·0, 1969, NASA TN D-5030.
13. MCGHEE, R.J. Jet-plume-induced flow separation on axisymmetric bodies at Mach numbers of 3·00, 4·50 and 6·00, 1970, NASA TM X-2059.
14. WU, J.M. and AOYAMA, K. Pressure distributions for axisymmetric bodies with discontinuous curvature in transonic flow, 1970, US Army Missile Command, Redstone Arsenal, Alabama, Technical Report RD-TR-70-25.
15. WU, J.M., AOYAMA, K. and MOULDEN, T.H. Transonic flow field calculation around ogive cylinders by non-linear-linear stretching method, 1970, US Army Missile Command, Redstone Arsenal, Alabama, Technical Report, RD-TR-70-12.
16. WU, J.M., AOYAMA, K. and MOULDEN, T.H. Transonic flow fields around various bodies of revolution including preliminary studies on viscous effects with and without plume-summary report, 1971, US Army Missile Command Report, RD-TR-71-12.
17. MATESANZ, A., VELAZQUEZ, A., PERALES, J.M. and SANTIAGO-PROWALD, J. Numerical simulation of base-flow/plume interaction, 1998, AIAA Paper 98-1597.
18. BANNINK, W.J., HOUTMAN, E.M. and BAKKER, P.G. Base flow/underexpanded exhaust plume interaction in a supersonic external flow, 1998, AIAA Paper 98-1598.

https://doi.org/10.1017/S0001924000000099 Published online by Cambridge University Press

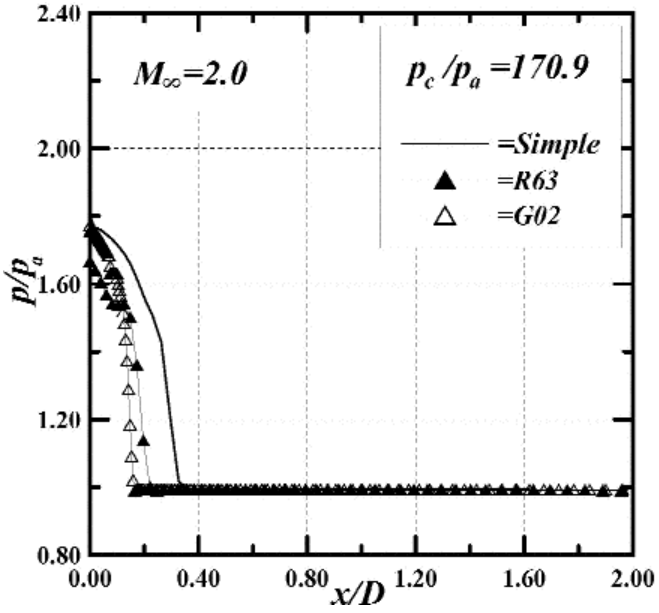


Figure 20. Pressure distributions on the afterbody of Model Simple, R63 and G02 at p_c/p_a = 170·9 and M_∞ = 2·0.

19. VENKATESWARAN, S., WEISS, J.M. and MERKLE, C.L. Propulsion related flowfields using the preconditioned Navier-Stokes equations, 1992, AIAA Paper 92-3437.
20. BARTH, T.J. and JESPERSEN, D. The design and application of upwind schemes on unstructured meshes, 1989, AIAA Technical Report 89-0366, AIAA 27th Aerospace Sciences Meeting, Reno, Nevada.
21. JAMESON, A., SCHMIDT, W. and TURKEL, E. Numerical solution of the Euler equations by finite volume methods using Runge-Kutta time-stepping schemes, 1981, AIAA Paper 81-1259.
22. BURT. J.R. An experimental investigation of the effect of several rocket plume simulators on the pressure distribution of a body of revolution at free stream Mach number of 0·9 to 1·2, 1970, US Army Missile Command, Redstone Arsenal, Alabama, Technical Report RD-TR-70-23.

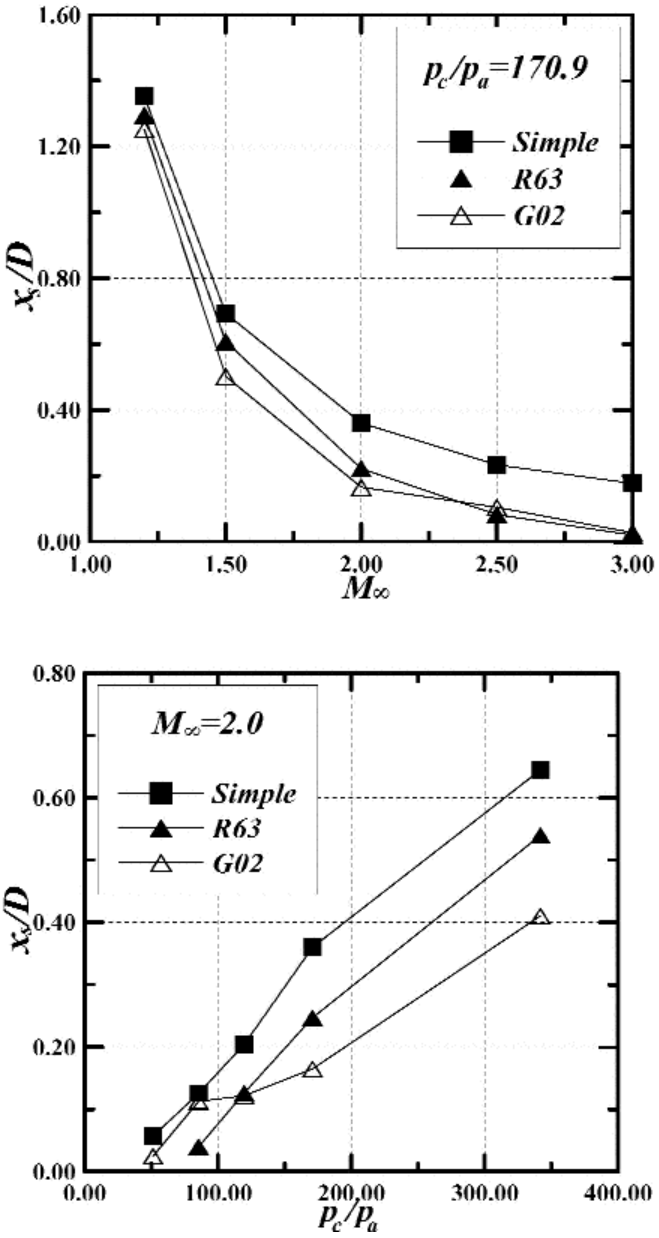


Figure 21. Comparison of shock positions for simple, rounded and grooved afterbodies: (a) Effect of Mach number, (b) Effect of plume pressure ratio.

https://doi.org/10.1017/S0001924000000099 Published online by Cambridge University Press